ChemComm

COMMUNICATION

View Article Online
View Journal | View Issue

Check for updates

Cite this: *Chem. Commun.*, 2026, **62**, 6572

Received 26th January 2026,
Accepted 23rd February 2026

DOI: 10.1039/d6cc00522e

rsc.li/chemcomm

Open Access Article. Published on 23 February 2026. Downloaded on 6/1/2026 8:42:52 AM.
This article is licensed under a Creative Commons Attribution-NonCommercial 3.0 Unported Licence.

Polarized Mo–O Units on g-C_3N_4 for enhanced photo-Fenton activity

Jun Zhao,†[a] Zhihao Li,†[a] Hongjian Deng,†[b] Wenjian Ma,[a] Hui Wang,*[a] Qun Zhang *[abc] and Xiaodong Zhang *[a]

Photo-Fenton technology is promising for organic wastewater treatment but suffers from poor charge separation and weak H_2O_2 activation. Here, we report a graphitic carbon nitride catalyst with polarized Mo–O units (CN-Mo-O). Spectroscopic analyses reveal that Mo–O units facilitate efficient charge separation and prolong carrier lifetime. Theoretical calculations indicate that polarized Mo–O centers lower the surface work function, accelerating H_2O_2 activation and superoxide radical generation. This synergistic regulation of photoexcited dynamics and surface activation enables excellent catalytic performance. This work demonstrates that coordination design of active centers effectively synchronizes photophysical and catalytic optimization.

Searching for effective protocols for organic-wastewater treatment has become a crucial prerequisite for ensuring sustainable societal development.[1,2] Since its first report in 1894,[3] the Fenton reaction (which involves redox reactions between Fe^{2+}/Fe^{3+} and H_2O_2 to generate reactive oxygen species (ROS) for pollutant degradation) has been widely applied in wastewater treatment.[4,5] As an integration of Fenton chemistry and photocatalysis, the ''photo-Fenton process'' not only accelerates the metal-ion redox cycles in catalysts but also offers advantages such as operational simplicity, environmental friendliness, and avoidance of secondary pollution.[6,7] For designing photo-Fenton catalysts, such integration requires synergistic regulation of catalytically active sites and photoexcitation properties.[8,9]

Atomically precise engineering has been a powerful pathway for designing advanced photocatalytic systems by integrating photoactive centers and catalytically active sites.[10–12] Catalysts with well-defined, atomically dispersed active sites possess tunable electronic structures and coordination environments. By precisely ''tailoring'' the coordination environment, such as tuning the types of coordinating atoms,[13] introducing adjacent vacancies,[14] adjusting electronic states,[15] or modifying geometric configurations,[16] it is possible to regulate reactant adsorption–desorption behavior, the activation efficiency of target molecules, charge separation kinetics, and excited-state electronic properties and lifetimes.[17,18] While traditional attention has focused on coordinated single-metal sites, the introduction of metal–oxygen (M–O) units provides additional degrees of freedom for electronic regulation. The inherently polarized character of the asymmetric M–O unit effectively tunes the electronic state of the metal center, accelerates charge separation and transfer, and optimizes the adsorption energy of key reaction intermediates.[19]

Graphitic carbon nitride (g-C_3N_4) is a metal-free conjugated polymer semiconductor. It has been demonstrated to be an ideal support for anchoring atomically dispersed active sites due to its versatile coordination environments, excellent chemical stability, and diverse sources.[20,21] In the present study, we constructed two types of atomically dispersed molybdenum sites on g-C_3N_4: a nitrogen-coordinated Mo site (CN-Mo) and a terminal-oxygen-coordinated Mo site (CN-Mo-O). This design aims to systematically tune the photoexcited-state properties of the catalysts (such as charge-separation efficiency and carrier lifetime) and reactive-site properties (such as adsorption and activation behavior) toward reactants.

Samples were prepared by controlling the calcination atmosphere. Then, the morphology and structure of the samples were first characterized by transmission electron microscopy (TEM), which revealed that CN, CN-Mo-O, and CN-Mo samples exhibited amorphous aggregate morphologies (Fig. S1a, S2 and S3a). Atomic-resolution high-angle annular dark-field scanning TEM (HAADF-STEM) (Fig. 1a and Fig. S3b) showed isolated bright dots in CN-Mo and CN-Mo-O, corresponding to individual Mo atoms. Energy-dispersive X-ray spectroscopy (EDS) elemental mapping confirmed the homogeneous distribution of Mo, C, and N (Fig. 1b and Fig. S3c). The X-ray diffraction (XRD) patterns in Fig. S4 give characteristic peaks at 13.1° and 27.4°, corresponding to the in-plane arrangement of

[a] *Hefei National Research Center for Physical Sciences at the Microscale, University of Science and Technology of China, Hefei, Anhui, 230026, China. E-mail: wanghuig@ustc.edu.cn, qunzh@ustc.edu.cn, zhxid@ustc.edu.cn*
[b] *Department of Chemical Physics, University of Science and Technology of China, Hefei, Anhui, 230026, China*
[c] *Hefei National Laboratory, University of Science and Technology of China, Hefei, Anhui, 230088, China*
† These authors contributed equally.

This journal is © The Royal Society of Chemistry 2026

Open Access Article. Published on 23 February 2026. Downloaded on 6/1/2026 8:42:52 AM.
This article is licensed under a Creative Commons Attribution-NonCommercial 3.0 Unported Licence.

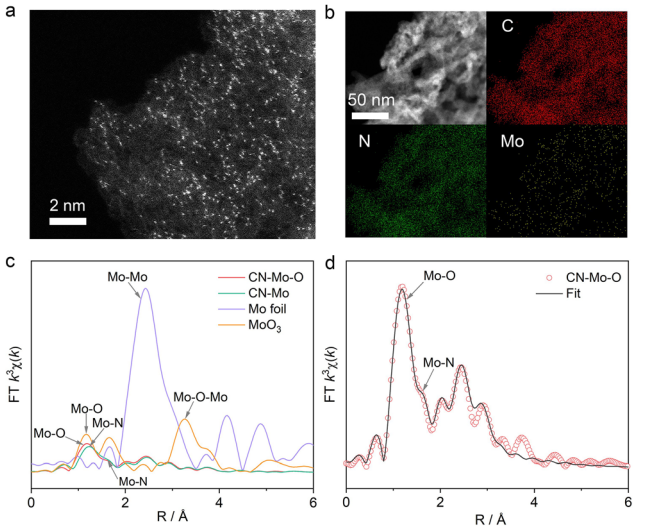

Fig. 1 (a) Atomic-resolution HAADF-STEM and (b) EDS mapping of CN-Mo-O. (c) FT-EXAFS curves of CN-Mo-O, CN-Mo, standard Mo-foil, and MoO_3 at the Mo K edge. (d) FT-EXAFS fitting curves of CN-Mo-O at the Mo K edge, which is the enlarged version of CN-Mo-O in Fig. 1c for better illustration.

tri-*s*-triazine units and graphene-like π–π layer-stacking structure, respectively.[22,23] Compared with that of pristine CN, the peak intensities of CN-Mo and CN-Mo-O were significantly reduced, indicating that Mo introduction might weaken the structural ordering of the carbon nitride matrix.[24] The characteristic stretching vibration bands of C–N heterocycles between 1200 and 1600 cm^{-1} in the Fourier-transform infrared (FT-IR) spectra (Fig. S5a) confirmed a maintained carbon nitride matrix after single-atom modification.[25,26] The bending vibration peak of the triazine ring around 809 cm^{-1} exhibited a pronounced red shift (Fig. S5b),[27] hinting at coordination interactions between Mo and N atoms in the CN framework. The thermogravimetric-differential scanning calorimetry (TG-DSC) revealed that single-atom incorporation reduced the thermal stability of the CN framework (Fig. S6). Nitrogen adsorption–desorption measurements indicated that the anchoring of Mo species effectively increased the specific surface area and optimized the pore structure (Fig. S7). X-ray photoelectron spectroscopy (XPS) (Fig. S8) confirmed Mo–N bond formation in CN-Mo and CN-Mo-O, indicating Mo incorporation. A new O 1s peak at 530.5 eV in CN-Mo-O (Fig. S8d) was assigned to Mo–O bonds, with lower binding energy than adsorbed or C–O oxygen, suggesting higher electron density. Mo 3d spectra (Fig. S8e) showed distinct Mo states. CN-Mo-O had more Mo^{6+} than CN-Mo, indicating that Mo–O bonds promoted Mo to a higher oxidation state. The Mo^{6+} $3d_{5/2}$ peak in CN-Mo-O exhibited a clear blue shift relative to CN-Mo, reflecting reduced local electron density, likely due to polarized Mo–O units.

X-ray absorption near-edge structure (XANES) and extended X-ray absorption fine structure (EXAFS) were used to probe the local coordination and electronic states of Mo. XANES spectra (Fig. S9) showed that the absorption edge energies of both samples lay between those of metallic Mo foil and MoO_3. In *k*-space (Fig. S10), CN-Mo and CN-Mo-O exhibited similar oscillations at 0–12 $Å^{-1}$, but CN-Mo-O resembled MoO_3 in the 12–14 $Å^{-1}$ region, suggesting a molybdenum oxide-like local environment. In the Fourier-transform (FT) R-space spectra (Fig. 1c), CN-Mo showed a dominant peak at 1.23 Å, corresponding to Mo–N coordination. In CN-Mo-O, a new peak appeared at 1.17 Å, consistent with Mo–O coordination in MoO_3. Although the bond lengths of Mo–O and Mo–N are similar,[22] XPS and spectral analyses confirmed that the main peak in CN-Mo arose from Mo–N, while the new peak in CN-Mo-O reflected the formation of Mo–O bonds. EXAFS fitting confirmed the coexistence of Mo–N and Mo–O bonds in CN-Mo-O, forming a composite structure of anchored Mo–N sites and surface Mo–O_x species (Fig. 1d). A weak feature near 3.5 Å indicated minor Mo–Mo metallic bonding, but HAADF-STEM confirmed that isolated Mo atoms dominated in both samples, and the trace clusters were not the dominant factor responsible for the performance differences between the two materials.

The photoexcitation properties of the samples were investigated by spectroscopy. Ultraviolet–visible (UV–vis) absorption spectra revealed that all samples displayed the intrinsic g-C_3N_4 band-edge absorption below 460 nm (Fig. S11), while CN-Mo and CN-Mo-O exhibited enhanced absorption in the visible–near-infrared region ($\lambda > 460$ nm) due to Mo coordination with the CN matrix. Steady-state photoluminescence (PL) spectroscopy demonstrated a substantial decrease in PL emission intensity in the order of CN, CN-Mo-O, and CN-Mo (Fig. 2a), and normalized PL spectra (Fig. S12) indicated different modulation of electronic energy levels by Mo–O and Mo. Time-resolved PL measurements showed average lifetimes of 1.65 ± 0.30 ns (CN), 2.16 ± 0.30 ns (CN-Mo-O), and 1.27 ± 0.30 ns (CN-Mo) (Fig. 2b, Table S1). The prolonged lifetime in CN-Mo-O suggested more efficient migration of photogenerated charge carriers to the surface for photo-Fenton reactions. Transient photocurrent measurements (Fig. S13) further confirmed that CN-Mo-O exhibited the highest photocurrent density, supporting its superior charge separation and transfer efficiency.

To investigate photogenerated carrier dynamics, femtosecond time-resolved transient absorption (fs-TA) spectroscopy was performed. Fig. S14 shows the fs-TA spectra of CN, CN-Mo-O, and CN-Mo. A broad negative signal between 440 nm and 600 nm (Fig. 2c) corresponded to the ground-state bleach (GSB), which is characteristic of g-C_3N_4-based materials and signifies the depopulation of the ground state due to photoexcitation. Attenuation of the GSB signal upon Mo-modification suggested rapid depletion of the photoexcited state, likely due to an ultrafast electron transfer process from the g-C_3N_4 framework to the incorporated Mo-species. Global analyses of kinetic traces at 480, 490, and 500 nm (Fig. 2d–f) revealed average lifetimes (τ_{ave}) of 239.80 ± 12.97 ps for CN, 24.10 ± 1.71 ps for CN-Mo-O, and 4.81 ± 0.28 ps for CN-Mo. The long lifetime in CN reflected slow exciton dissociation and limited charge separation. In CN-Mo, the markedly shortened lifetime indicated that Mo sites efficiently promoted exciton dissociation. However, the concurrently short PL lifetime suggested that these sites also introduced strong non-radiative recombination channels, rapidly annihilating photogenerated carriers and limiting their participation in surface reactions. In contrast,

Open Access Article. Published on 23 February 2026. Downloaded on 6/1/2026 8:42:52 AM.
This article is licensed under a Creative Commons Attribution-NonCommercial 3.0 Unported Licence.

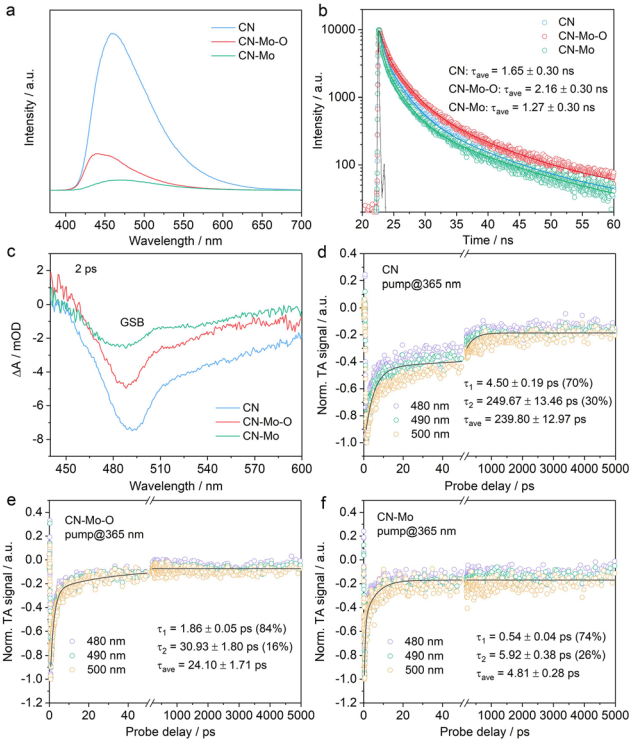

Fig. 2 (a) Steady-state and (b) time-resolved PL spectra of CN, CN-Mo-O, and CN-Mo. (c) Representative fs-TA spectra taken at the 2-ps probe delay for the three samples, along with the corresponding kinetic traces of (d) CN, (e) CN-Mo-O, and (f) CN-Mo.

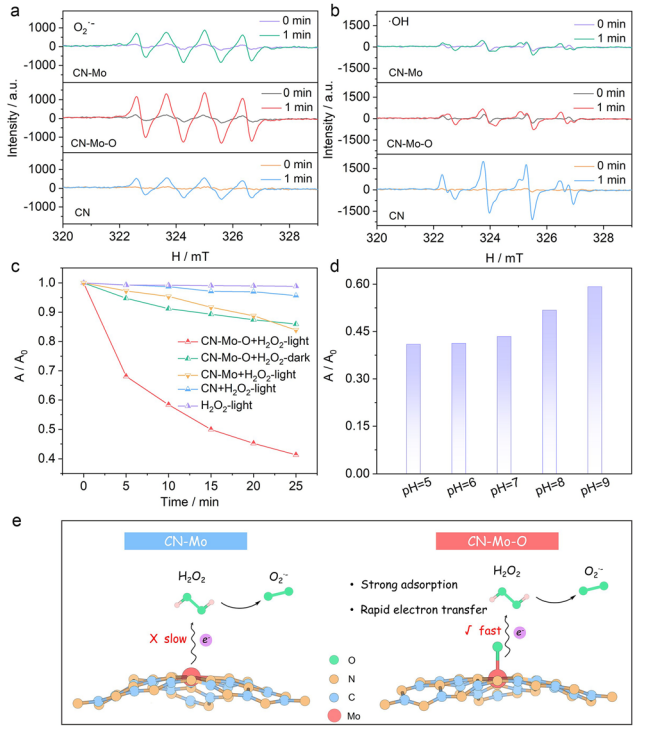

Fig. 3 EPR spectra of CN, CN-Mo-O, and CN-Mo/visible photo-Fenton systems for trapping (a) $^{\bullet}O_2^-$ and (b) $^{\bullet}$OH. (c) Photo-Fenton catalytic methyl-orange degradation in different systems (catalyst dose = 0.2 mg mL^{-1}; $[H_2O_2]$ = 50 μM; [methyl orange] = 20 mg L^{-1}). (d) pH-dependent CN-Mo-O-based photo-Fenton catalytic methyl-orange degradation. (e) H_2O_2 activation (schematic).

the Mo–O structure in CN-Mo-O accelerates exciton-to-charge conversion and suppresses non-radiative recombination, providing more long-lived free carriers for surface catalysis.

According to the analyses stated above, we anticipated CN-Mo-O to hold superior photo-Fenton catalytic capacity. Electron paramagnetic resonance (EPR) spectroscopy was carried out to examine ROS generation during the photo-Fenton process. As shown in Fig. 3a, CN-Mo-O–H_2O_2 and CN-Mo–H_2O_2 produced weak DMPO–$^{\bullet}O_2^-$ signals in the dark, indicating slow H_2O_2 activation at Mo sites. Under illumination, all samples showed stronger signals, while CN-Mo-O–H_2O_2 displayed the highest intensity, confirming its superior ability to generate $^{\bullet}O_2^-$. EPR measurements for $^{\bullet}$OH detection (Fig. 3b) showed weak DMPO–$^{\bullet}$OH signals in the dark and no meaningful increase under light, suggesting that H_2O_2 activation at Mo sites mainly yielded $^{\bullet}O_2^-$ rather than $^{\bullet}$OH. The minor deviant signals detected may have originated from interference by short-lived $^{\bullet}O_2^-$ species. This observation aligns with reports that Mo species favor $^{\bullet}O_2^-$ formation through reactions with multiple H_2O_2 molecules.[28] We further quantified ROS using molecular probes. After illumination for 10 min, the CN-Mo-O-H_2O_2 system generated the most $^{\bullet}O_2^-$ (Fig. S15a), while producing almost no $^{\bullet}$OH (Fig. S15b). These results agreed with EPR data, confirming that CN-Mo-O selectively and efficiently generated $^{\bullet}O_2^-$.

Methyl orange is used as a "model" pollutant to evaluate photo-Fenton catalytic performance. Under visible light, CN-Mo-O achieved 60% degradation in 25 min, significantly outperforming CN-Mo (16%) and CN (5%) (Fig. 3c). In the dark, CN-Mo-O degraded only 14% of methyl orange, highlighting the essential role of light. Without H_2O_2, the photocatalytic efficiency of CN-Mo-O was 17% (Fig. S16), confirming the critical role of H_2O_2. Apparent rate constants (k) further quantified this trend (Fig. S17). CN-Mo-O exhibited the highest k (0.0322 min^{-1}), 4.7- and 17.9-times those of CN-Mo (0.0068 min^{-1}) and CN (0.0018 min^{-1}), respectively. These results confirmed the superior photo-Fenton activity of CN-Mo-O. Quenching experiments identified $^{\bullet}O_2^-$ as the main driver of methyl orange degradation by CN-Mo-O (Fig. S18). Catalyst dose and the H_2O_2 concentration were further optimized (Fig. S19). The CN-Mo-O system maintained high degradation efficiency over a pH range of 5–9 (Fig. 3d) and retained stable activity after six consecutive cycles (Fig. S20), demonstrating good adaptability and reusability. Open-circuit potential measurements showed that CN-Mo-O had the strongest H_2O_2 adsorption, while the potential change under light indicated a transition from simple adsorption to an efficient catalytic cycle with rapid electron transfer and H_2O_2 activation (Fig. S21, 3e).

To clarify the electronic structure modulation of the Mo single-atom site by O coordination and its role in the photo-Fenton reaction, computational models of CN-Mo and CN-Mo-O were constructed (Fig. S22), and DFT calculations were performed, including density of states (DOS), differential charge density, Bader charge, and work function analyses. The DOS comparison showed that in CN-Mo, the Mo states

This journal is © The Royal Society of Chemistry 2026

Open Access Article. Published on 23 February 2026. Downloaded on 6/1/2026 8:42:52 AM.
This article is licensed under a Creative Commons Attribution-NonCommercial 3.0 Unported Licence.

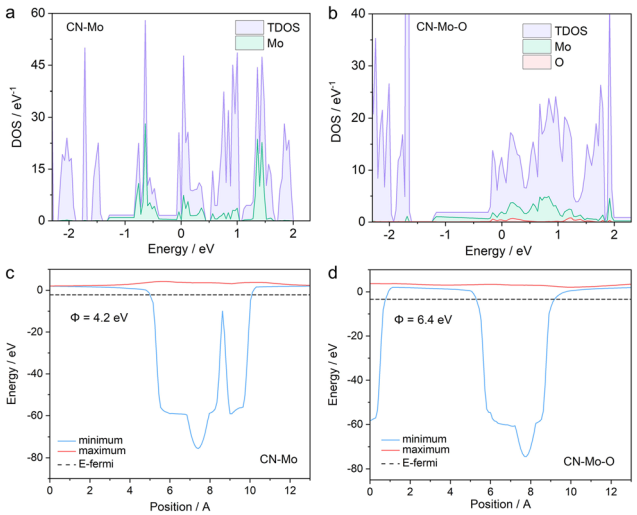

Fig. 4 Calculated DOS of (a) CN-Mo and (b) CN-Mo-O. Work functions (Φ) of (c) CN-Mo and (d) CN-Mo-O.

constituted a significant component within the valence band (Fig. 4a). In contrast, for CN-Mo-O (Fig. 4b), the contribution of the Mo d-orbitals shifted markedly above the Fermi level into the conduction band region, and the O atom formed distinct features near the bottom of the conduction band. This electronic reconstruction created a hybridized conduction band with acceptor character, enabling more efficient electron capture and transfer from the CN matrix. Charge density difference maps showed electron accumulation around the O atom in the Mo–O unit (Fig. S23a and b). Bader charge analyses showed that Mo in CN-Mo-O had 11.92 *e*, while the coordinated O had 6.99 *e*. Compared with the Mo charge in CN-Mo (12.77 *e*), the electron population on Mo (14 *e*, Mo_sv pseudopotential) was reduced further (Fig. S23c and d). This indicated significant electron transfer from Mo to O, thereby forming a polarized $Mo^{\delta+}$–$O^{\delta-}$ unit in CN-Mo-O. The electron-deficient $Mo^{\delta+}$ can act as a Lewis acid site, anchoring the oxygen of H_2O_2 *via* electrostatic and electrophilic interactions, which stabilizes adsorption and promotes interfacial electron transfer. Work function (Φ) calculations revealed that CN-Mo-O had a lower Φ than CN-Mo (Fig. 4c and d), indicating a stronger tendency to donate electrons. This provides favorable initial thermodynamic conditions for the Mo site to act as an electron donor and drive subsequent H_2O_2 heterolysis reactions. Overall, O coordination modulates the Mo electronic structure, enhances electron capture, and, by forming a polarized unit and lowering the work function, synergistically optimizes H_2O_2 adsorption and activation.

This work shows tailoring Mo coordination in photo-Fenton catalysts synergistically regulates photoexcitation and surface reactivity. In CN-Mo-O, the polarized Mo–O units enhance charge separation and prolong carrier lifetime. They also form $Mo^{\delta+}$–$O^{\delta-}$ centers with a lowered work function, enabling efficient electron transfer. This enables superior photo-Fenton activity and selective superoxide radical generation. This work highlights coordination-directed design as a generalizable strategy to advance the efficiency of heterogeneous photo-Fenton systems.

Conflicts of interest

There are no conflicts of interest to declare.

Data availability

The authors declare that the data supporting the conclusions reached from our study are available within the manuscript and its supplementary information (SI) files. Supplementary information includes TEM, HAADF-STEM, and elemental mapping images; XRD patterns; FT-IR spectra; TGA and DSC curves; BET and pore-size distribution analyses; XPS, XANES, and EXAFS spectra; UV–vis and normalized steady-state PL spectra; periodic on/off photocurrent responses and EIS; contour maps of fs-TA; detection of $\bullet O_2^-$ and •OH; apparent rate constants; cycling tests; open-circuit potential measurements; differential charge density map and Bader charges; as well as experimental details and additional data analyses. See DOI: https://doi.org/10.1039/d6cc00522e.

Acknowledgements

This work was supported by the National Key R&D Program of China (2022YFA1502903), the CAS Project for Young Scientists in Basic Research (YSBR-142), the Fundamental Research Funds for Central Universities (WK2060250115), the National Natural Science Foundation of China (22275179, 92477116, and 22173090), the Innovation Program for Quantum Science and Technology (2021ZD0303303), and the Anhui Initiative in Quantum Information Technologies (AHY090200). This work was partially carried out at the Instruments Center for Physical Science, University of Science and Technology of China. Numerical calculations were conducted at the Supercomputing Center of the University of Science and Technology of China.

References

1 C. Dong, J. Ji, B. Shen, M. Xing and J. Zhang, *Environ. Sci. Technol.*, 2018, **52**, 11297–11308.
2 J. Miao, J. Song, J. Lang, Y. Zhu, J. Dai, Y. Wei, M. Long, Z. Shao, B. Zhou, P. J. J. Alvarez and L. Zhang, *Environ. Sci. Technol.*, 2023, **57**, 4266–4275.
3 S. Goldstein, D. Meyerstein and G. Czapski, *Free Radical Biol. Med.*, 1993, **15**, 435–445.
4 S. Liang, L. Zhu, J. Hua, W. Duan, P.-T. Yang, S.-L. Wang, C. Wei, C. Liu and C. Feng, *Environ. Sci. Technol.*, 2020, **54**, 6406–6414.
5 Y. Yin, L. Shi, W. Li, X. Li, H. Wu, Z. Ao, W. Tian, S. Liu, S. Wang and H. Sun, *Environ. Sci. Technol.*, 2019, **53**, 11391–11400.
6 W. Liu, P. Wang, J. Chen, X. Gao, H. Che, X. Su, B. Liu and Y. Ao, *Environ. Sci. Technol.*, 2024, **20**, 100414.
7 S. Wang, X. Li, C. Yuan, Z. Sun, Y. Lu, S. Pei, Y. Wu, C.-C. Wang and B. Wang, *Appl. Catal., B*, 2025, **379**, 125717.
8 X. He, X. Zhong, L. Li, S. Shang, W. Si, H. Wang, X. Zhang and Y. Xie, *CCS Chem.*, 2025, **7**, 843–853.
9 J. Zhao, H. Li, Z. Li, S. Jiang, M. Guan, P. Zhang, S. Shang, Z. Zhao, H. Wang, Q. Zhang, X. Zhang and Y. Xie, *Natl. Sci. Rev.*, 2025, **12**, nwaf062.
10 B. Wang, H. Cai and S. Shen, *Small Methods*, 2019, **3**, 1800447.
11 N. Martín and F. G. Cirujano, *ChemCatChem*, 2021, **13**, 2751–2765.
12 C. Gao, J. Low, R. Long, T. Kong, J. Zhu and Y. Xiong, *Chem. Rev.*, 2020, **120**, 12175–12216.
13 X. Zhang, X. Guo, H. Jiao, Y. Wang, H. Li, X. Lian, H. Wang, Y. Zhang, X. Chang, J. Zhang and X.-H. Bu, *ACS Nano*, 2025, **19**, 39491–39506.

Open Access Article. Published on 23 February 2026. Downloaded on 6/1/2026 8:42:52 AM.
This article is licensed under a Creative Commons Attribution-NonCommercial 3.0 Unported Licence.

14 J. Shen, C. Luo, S. Qiao, Y. Chen, Y. Tang, J. Xu, K. Fu, D. Yuan, H. Tang, H. Zhang and C. Liu, *ACS Catal.*, 2023, **13**, 6280–6288.
15 S. Jin, W. Tan, Y. Huang, Y. Wang, Z. He, H. Zhang, S. Song, Y. Cai and T. Zeng, *Nat. Commun.*, 2025, **16**, 10455.
16 C. Fu, Y. Wang, L. Xu, Q. Shui, Q. Zhang, R. Zhong, Z. Sun, W. Chen, Y. Wei, H. Liu, G. Zhao and Y. Li, *J. Am. Chem. Soc.*, 2026, **148**, 280–291.
17 R. Sun, X. Cao, J. Ma, H.-C. Chen, C. Chen, Q. Peng and Y. Li, *Nature Synth.*, 2025, **4**, 965–975.
18 Z. Lian, F. Gao, H. Xiao, D. Luo, M. Li, D. Fang, Y. Yang, J. Zi and H. Li, *Angew. Chem. Int. Ed.*, 2024, **63**, e202318927.
19 C. Ye, H. Cheng, L. Zheng, J. Lin, Q. Xu, Y. Qiu, Z. Pan and Y. Qiu, *Nano Lett.*, 2023, **23**, 1573–1581.
20 G. F. S. R. Rocha, M. A. R. da Silva, A. Rogolino, G. A. A. Diab, L. F. G. Noleto, M. Antonietti and I. F. Teixeira, *Chem. Soc. Rev.*, 2023, **52**, 4878–4932.
21 Y. Shi, X. Hai, L. Cheng, H. Du, X. Yu, H. T. Ang, J. Wu, J. Chen, G. Wang, J. Lu and J. Wu, *Nat. Catal.*, 2025, **8**, 1325–1337.
22 J. Fu, J. Yu, C. Jiang and B. Cheng, *Adv. Energy Mater.*, 2018, **8**, 1701503.
23 C. Zhang, D. Qin, Y. Zhou, F. Qin, H. Wang, W. Wang, Y. Yang and G. Zeng, *Appl. Catal., B*, 2022, **303**, 120904.
24 R. Zhang, P. Li, F. Wang, L. Ye, A. Gaur, Z. Huang, Z. Zhao, Y. Bai and Y. Zhou, *Appl. Catal., B*, 2019, **250**, 273–279.
25 M. Chen, J. Wu, C. Lu, X. Luo, Y. Huang, B. Jin, H. Gao, X. Zhang, M. Argyle and Z. Liang, *Green Energy Environ.*, 2021, **6**, 938–951.
26 Y. Chen, F. Ding, A. Khaing, D. Yang and Z. Jiang, *Appl. Surf. Sci.*, 2019, **479**, 757–764.
27 S. Zhang, C. Hu, H. Ji, L. Zhang and F. Li, *Appl. Surf. Sci.*, 2019, **478**, 304–312.
28 I. Popivker, I. Zilbermann, E. Maimon, H. Cohen and D. Meyerstein, *Dalton Trans.*, 2013, **42**, 16666–16668.

 This journal is © The Royal Society of Chemistry 2026